A&A 413, 1163–1175 (2004)
DOI: 10.1051/0004-6361:20031564

Astronomy & Astrophysics

Properties of the nuclei of Centaurs Chiron and Chariklo

O. Groussin, P. Lamy, and L. Jorda

Laboratoire d'Astronomie Spatiale, BP 8, 13376 Marseille Cedex 12, France

Received 12 February 2003 / Accepted 30 September 2003

Abstract. We analyze visible, infrared, radio and spectroscopic observations of 2060 Chiron in a synthetic way to determine the physical properties of its nucleus. From visible observations performed from 1969 to 2001, we determine an absolute V magnitude for the nucleus of 7.28 ± 0.08 with an amplitude of 0.16 ± 0.03, implying a nearly spherical nucleus with a ratio of semi-axes $a/b = 1.16 \pm 0.03$. Infrared observations at 25, 60, 100 and 160 μm (i.e., covering the broad maximum of the spectral energy distribution) obtained with the Infrared Space Observatory Photometer (ISOPHOT) in June 1996 when Chiron was near its perihelion are analyzed with a thermal model which considers an intimate mixture of water ice and refractory materials and includes heat conduction into the interior of the nucleus. We find a very low thermal inertia of 3^{+5}_{-3} J K^{-1} m^{-2} s$^{-1/2}$ and a radius of 71 ± 5 km. Combining the visible and infrared observations, we derive a geometric albedo of 0.11 ± 0.02. We find that the observed spectra of Chiron can be fitted by a mixture of water ice (∼30%) and refractory (∼70%) grains, and that this surface model has a geometric albedo consistent with the above value. We also analyze the visible, infrared and radio observations of Chariklo (1997 CU26) and derive a radius of 118 ± 6 km, a geometric albedo of 0.07 ± 0.01 and a thermal inertia of 0^{+2}_{-0} J K^{-1} m^{-2} s$^{-1/2}$. A mixture of water ice (∼20%) and refractory (∼80%) grains is compatible with the near-infrared spectrum and the above albedo.

Key words. minor planets, asteroids

1. Introduction

2060 Chiron (hereafter Chiron) is a transition object between the Kuiper belt objects and the Jupiter family comets (Kowall 1996). Its semimajor axis $a = 13.620$ AU classifies it in the Centaur family, with an orbit between Jupiter ($a = 5$ AU) and Neptune ($a = 30$ AU). Chiron is actually one of the few Centaurs which displays activity (Tholen et al. 1988) together with, for example, P/Oterma, P/Schwassmann-Wachmann 1 and C/NEAT (2001 T4) (Bauer et al. 2003). It has therefore attracted considerable interest, in particular during its perihelion passage (15 Feb. 1996, at $q = 8.45$ AU), because it was anticipated that its activity would increase. From the numerous observations carried out so far and which will be later discussed in detail, it emerges the picture of a body having the following properties. The radius determinations vary from 74 to 104 km. The synodic rotation period is well determined and was equal to 5.917813 ± 0.000007 h on January 1991 (Marcialis & Buratti 1993). The short period lightcurve patterns detected by Marcialis & Buratti (1993) "*probably are due to an irregular or faceted body, and they offer evidence that Chiron currently presents an approximately equatorial aspect to the Earth*". Moreover, the amplitude of the lightcurve indicates a quasi-spherical body. The geometric albedo of the nucleus is $0.14^{+0.06}_{-0.03}$ (Campins et al. 1994) which is larger than the range of 0.04 ± 0.02 found for other cometary nuclei (Lamy et al. 2004). The spectrum of Chiron is featureless and quite flat in the 0.5−0.9 μm range, although variations of a few percents in the slope of the spectral reflectivity can occur (Lazzaro et al. 1997). Recent publications by Foster et al. (1999) and Luu et al. (2000) reported the detection of water ice on the basis of absorption features near 2.0 μm. A similar result already obtained on Pholus and Chariklo (1997 CU26) suggests that water ice is probably ubiquitous on the surface of Centaurs (Brown 2000). During the 1987 to 1990 interval, when Chiron was beyond 11 AU from the Sun, a large brightening was observed which is not yet very well understood. At such a heliocentric distance, the activity is believed to be dominated by the sublimation of CO (Capria et al. 1996).

In this paper, we analyze visible, infrared, radio and spectroscopic observations of 2060 Chiron in a synthetic way to determined the physical properties of its nucleus. In Sect. 2, we first summarize observations of Chiron at visible, infrared (including unique ISOPHOT observations at 25, 60, 100 and 160 μm) and radio wavelengths and by stellar occultation, discussing the results of each approach and their limitations. In Sect. 3, we explain in detail our thermal model used to interpret the infrared observations, which includes dust, water ice and heat conduction into the interior of the nucleus. In Sect. 4, we discuss the results: thermal inertia, radius, geometric albedo, reflectance of the nucleus, composition of the surface, contribution of the coma to the visible and infrared fluxes, and

Send offprint requests to: O. Groussin,
e-mail: olivier.groussin@oamp.fr

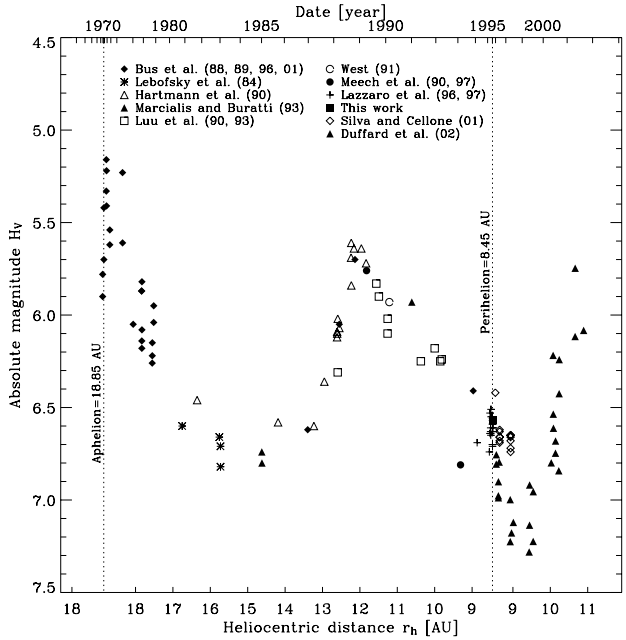

Fig. 1. Absolute magnitudes H_v of Chiron as a function of heliocentric distance and time.

comparison of our model with previous infrared observations. In Sect. 5, we extend our analysis to the Centaur Chariklo (1997 CU26).

2. Summary of observations and results

2.1. Visible observations

Figure 1 summarizes measurements of the magnitude of Chiron performed between September 1969 and August 2001. We favored the V magnitudes when available, otherwise we converted the R magnitudes using $V - R = 0.37$ (Hartmann et al. 1990). This quasi-solar color correction is justified by the neutral spectrum of Chiron obtained in June 1996 by Lazzaro et al. (1997). Our observation was performed with the Danish 1.54 m telescope at ESO, La Silla, in support of the ISOPHOT observations performed 10 days before. Several images were acquired through the R filter on 1996 June 25.02 UT, when the comet was at a helicentric distance of 8.468 AU and a geocentric distance of 8.326 AU. Standard stars from the Landolt field PG1323-086 (Landholt 1992) were used to perform an absolute calibration of the images. We obtained a magnitude $R = 15.79 \pm 0.03$ which we converted to $V = 16.16 \pm 0.03$ with the above color index.

The derivation of the absolute magnitude $H_v = V(1, 1, 0)$ requires a correction for the phase effect. From their observations of December 1986 which covered a very small range of phase angles (1.05° to 1.62°) and using the (H, G) formalism, Bus et al. (1989) derived a value $G = 0.7$. But later in 1996, when Chiron was at a comparable level of activity, Lazzaro et al. (1997) determined a very different value, $G = 0.42$. We do concur with Lazzaro et al. (1996) that the correction for the phase effect poses a problem because of the activity of Chiron resulting in a variable coma and that the (H, G) formalism may not be appropriate in this case. In view of this situation, we decided to adopt the simple linear phase function with a coefficient $\beta = 0.05 \pm 0.01$ mag deg^{-1}, typical of cometary nuclei and also consistent with the data of Bus et al. (1989). We applied this phase correction to the whole set of observations plotted in Fig. 1. In this present study, the above problem is alleviated by the fact that we focus our attention to the faintest magnitudes of Chiron, hopefully reflecting a situation where the coma was negligibly faint. Moreover, the difference between H_v calculated with $G = 0.7$ or $\beta = 0.05$ mag/deg is lower than 2% for Chiron as the phase angle is always $\leq 7°$.

As illustrated by the variations of H_v with heliocentric distance (Fig. 1), Chiron underwent considerable variations of its activity, with a general trend totally uncorrelated with its heliocentric distance. A long phase of activity took place before 1978, fully documented by Bus et al. (2001). Beginning at some unknown time prior to the earliest observations in 1969, the brightness of Chiron reached a peak by late 1972, about two years after aphelion and was then ~0.4 mag brighter than at the second outburst of 1989. Following the 1972 peak, the activity gradually decreased so that a minimum was reached between 14 and 16 AU. It then resumed quite rapidly to reach a maximum at 12.5 AU in September 1988 and then progressively decayed. Chiron was still active at perihelion (8.45 AU). Post-perihelion, the decrease of activity continued and Chiron reached what appears to be its absolute minimum of activity in June 1997 with $H_v = 7.28$, i.e. 0.5 magnitude lower than the minimum of 6.8 reached at 14–16 AU pre-perihelion. This therefore yields the best estimate of the magnitude of the nucleus. Next, the activity increased again very rapidly and the magnitude reached 5.75 on April 2001. The whole set of data displays conspicuous "short-term" variations of the activity which can reach 0.3–0.4 mag over a few months.

The large outbursts which culminated at 12.5 AU pre-perihelion and 10.5 AU post-perihelion as well as the aphelion outburst are not well understood. Water ice does not sublimate beyond 6 AU and CO and/or CO_2 must probably be invoked to explain such an activity at large heliocentric distances (Capria et al. 1996). CO has indeed been marginally detected in June 1995 when Chiron was at 8.50 AU from the Sun by Womack & Stern (1997) who derived a production rate of $1.5 \pm 0.8 \times 10^{28}$ s^{-1}. Rauer et al. (1997) derived an upper limit of 1.0×10^{28} s^{-1} for the CO production rate near perihelion. Different mechanisms have been proposed: a heat wave reaching the CO sublimation front (Schmitt et al. 1991), shape and/or albedo effects on the surface of the nucleus and mantle disruption (Johnson 1991). The most comprehensive work to explain the activity variations of Chiron was performed by Duffard et al. (2002): using a model for the coma developed by Meech & Belton (1990) and assuming a long lifetime of 1400 days for the particules in the coma, they could fit all the photometric data over 30 yr. According to this model, outbursts could be produced by the gas outflow of CO, CO_2, or another element of similar volatility from an active region.

The question of the detection of the nucleus of Chiron can also be approached by considering its rotational lightcurve, as its variation with a period of 5.92 h is correctly attributed to a spinning, non-spherical solid body. Since the direction of the spin axis is not expected to change, the long-term change in

Table 1. Absolute magnitudes H_v and magnitude variations Δm_v of the lightcurve of Chiron.

Date	H_v	Δm_v	Ref.
1985 Jan. 19	6.80	>0.05	(1)
1986 Dec.	6.62	0.088 ± 0.003	(2)
1988 Feb. 29	6.31	0.08 ± 0.01	(3)
1988 Oct. 31	5.70	0.04 ± 0.01	(4)
1989 Apr. 11	5.76	0.04 ± 0.01	(5)
1990 Jan. 29-30	6.10	0.045 ± 0.005	(3)
1990 Feb. 21-24	5.93	0.05 ± 0.01	(6)
1991 Jan. 08	5.93	0.04 ± 0.01	(1)
1993 Feb. 20	6.81	∼0.02	(7)
1996 Jan.-Jun.	6.62	0.06 ± 0.01	(8)

References: (1) Marcialis & Buratti (1993); (2) Bus et al. (1989); (3) Luu & Jewitt (1990); (4) Bus & Bowell (1988); (5) Meech & Belton (1990); (6) West (1991); (7) Meech et al. (1997); (8) Lazzaro et al. (1997).

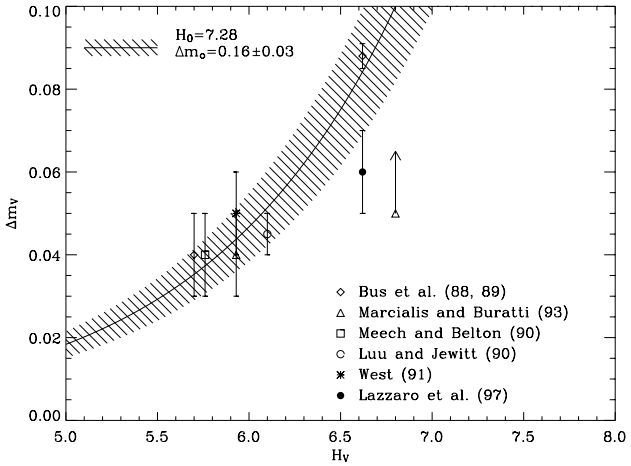

Fig. 2. The amplitude of the lightcurve Δm_v of Chiron as a function of the absolute magnitude H_v. The data points are the observations reported in Table 1 (except those of 29 February 1988 and 20 February 1993).

the amplitude Δm_v of the lightcurve of Chiron (nucleus+coma) can be unambiguously attributed to the varying level of the coma. This can be verified by the excellent anti-correlation between Δm_v and H_v as summarized in Table 1, with the exceptions of the 29 February 1988 and 20 February 1993 observations. The first observation (19 January 1985) gave a lower limit as it missed the extrema of the lightcurve. The formal method to analyze Δm_v was presented by Luu & Jewitt (1990) who derived a formula relating Δm_v, H_v, the absolute magnitude H_0 of the nucleus and the amplitude of its lightcurve Δm_0:

$$\Delta m_v = H_0 - H_v - 2.5 \log \left[10^{0.4(H_0 - H_v)} + 10^{-0.4 \Delta m_0} - 1 \right]. \quad (1)$$

The analysis of the observations reported in Table 1 (with the exceptions noted above) is performed using the Δm_v-H_v diagram (Fig. 2) where Δm_0 and H_0 are the two free parameters. Δm_0 can be estimated from the largest amplitude Δm_v = 0.09 ± 0.01 reported by Bus et al. (1989). The corresponding H_v = 6.62 indicates that a coma was still present so that we must choose a larger value for the nucleus. Adopting the faintest measured magnitude (Fig. 1) for the magnitude of the nucleus, i.e., $H_0 = 7.28 \pm 0.08$, we found that $\Delta m_0 = 0.16 \pm 0.03$ is the best value that fits all the observations of Fig. 2, using a χ^2 test. The errors bar of 0.03 on Δm_0 is calculated in order to fit all the measurements at the 1 σ level. Our value $\Delta m_0 = 0.16 \pm 0.03$ together with the consideration of Marcialis & Buratti (1993) that "*Chiron currently presents an approximately equatorial aspect to the Earth*", indicates a nearly spherical nucleus with a ratio of semi-axes $a/b = 1.16 \pm 0.03$, assuming a uniform albedo distribution. Moreover, as the inclination of Chiron is low (6.9°) and as it was observed far from the Earth by Marcialis & Buratti ($\Delta \sim 14$ AU), we conclude that its pole is approximately perpendicular to its orbital plane.

2.2. Infrared and radio observations

Table 2 summarizes the infrared and radio observations of Chiron. The results are separated in three different wavelength intervals: 10−25 μm for the mid-infrared, 25−160 μm for the far-infrared and 800−1200 μm for the radio (submillimetric and millimetric) domains. There is no observations between 160 and 800 μm.

The first interval 10−25 μm is in the Wien region of the spectral energy distribution (SED) for an expected color temperature of 120 K (Campins et al. 1994). Observations in this range were first performed by Lebofsky et al. (1984) at 22.5 μm, later by Campins et al. (1994) between 10.6 and 20.0 μm, and recently by Fernandez et al. (2002) at 12.5 and 17.9 μm. Altogether, these observations lead to a large range of radius values, between 70 and 104 km (Table 3).

The second interval 25−160 μm contains the maximum of the SED. The IRAS observations performed in 1983 at 25 and 60 μm (Sykes & Walker 1991) did not detect Chiron but allow to set an upper limit for the radius of 186 km. Chiron was later unambigously detected thanks to observations performed with the ISOPHOT photometer aboard the ISO satellite from 8 to 15 June 1996 (Peschke 1997). Chiron was then near perihelion at a heliocentric distance of 8.46 AU, thus maximizing its thermal emission. Four filters centered at 25, 60, 100 and 160 μm were used. We calculated the average of the infrared fluxes over the three nights of observation, weighted by the error on the flux for each wavelength and normalized to Δ = 8.15 AU (the difference on r_h and α is marginal), and we obtained 289 ± 51 mJy, 369 ± 109 mJy, 170 ± 67 mJy and 28 ± 15 mJy at 25 μm, 60 μm, 100 μm and 160 μm respectively. The error-bars reflect the statistical errors derived with the ISOPHOT Interactive Analysis software (PIA) and the current absolute calibration accuracy of 30% of the detectors. The fluxes at 160 μm must be considered with caution. Measurements of faint point sources with ISOPHOT at this wavelength were exceedingly difficult because of the sky confusion noise (Kiss et al. 2001). The real uncertainty on those measurements is therefore larger than the formal values given in Table 2. The ISOPHOT observations at 25, 60 and 100 μm are particulary well suited to determine the radius of Chiron,

Table 2. Infrared and radio observations of Chiron

Date	r_h^a [AU]	Δ^b [AU]	α^c [°]	λ^d [μm]	Flux [mJy]	Ref.
09 Jan. 1983	15.8	15.2	3	22.5	17 ± 9	(1)
18 Nov. 1991	10.0	9.7	5	19.2	$84 \pm 28^\dagger$	(2)
22 Nov. 1993	8.9	9.0	6	10.8	$15 \pm 4^\dagger$	(2)
				19.2	$298 \pm 59^\dagger$	(2)
31 Mar. 1994	8.8	8.0	4	10.6	$21 \pm 3^\dagger$	(2)
				20.0	$327 \pm 100^\dagger$	(2)
21 Jun. 2000	10.11	9.14	1.79	12.5	14.4 ± 1.18	(3)
				12.5	18.2 ± 2.7	(3)
23 Jun. 2000	10.11	9.15	1.98	12.5	14.3 ± 1.7	(3)
				17.9	43.9 ± 15.9	(3)
				17.9	56.4 ± 16.8	(3)
16 Sep. 1983	15.36	14.99	3.53	25	<80	(4)
				60	<135	(4)
08 Jun. 1996	8.46	8.06	6.45	25	284 ± 13	(5)
				60	388 ± 150	(5)
				100	178 ± 101	(5)
				160	48 ± 25	(5)
14 Jun. 1996	8.46	8.15	6.66	25	350 ± 17	(5)
				60	389 ± 158	(5)
				100	217 ± 108	(5)
				160	21 ± 23	(5)
15 Jun. 1996	8.46	8.16	6.69	25	262 ± 17	(5)
				60	339 ± 157	(5)
				100	128 ± 107	(5)
				160	22 ± 23	(5)
Averages for Jun. 1996*	8.46	8.15	6.66	25	289 ± 51	(6)
				60	369 ± 109	(6)
				100	170 ± 67	(6)
				160	28 ± 15	(6)
22 Mar. 1991‡	10.48	10.09	5.1	800	<11.1	(7)
27 Apr. 1994	8.79	8.29	5.8	1200	2.40 ± 0.55	(8)

[a] Heliocentric distance. [b] Geocentric distance. [c] Phase angle in degrees. [d] Wavelength. † The value is corrected to a monochromatic flux as defined in Campins et al. (1994). * Averages of the ISOPHOT observations. ‡ This is a combined value of the 04 Nov. 1990 and the 22 Mar. 1991 observations.

References: (1) Lebofsky et al. (1984); (2) Campins et al. (1994); (3) Fernandez et al. (2002); (4) Sykes & Walker (1991); (5) Peschke (1997); (6) This work; (7) Jewitt & Luu (1992); (8) Altenhoff & Stumpff (1995).

as they cover the maximum of the SED. The interpretation of these ISOPHOT observations, which has not yet been done, is presented in Sect. 4.

The last wavelength interval 800−1200 μm corresponds to the Rayleigh-Jeans regime where the flux is proportional to λ^{-2}. The observations are very difficult to perform, because the expected signal is very low. The main advantage of these measurements resides in their low sensitivity to the color temperature of the body, that is to the thermal model. Jewitt & Luu (1992) could not detect Chiron at 800 μm, and they gave a 3σ upper limit of 150 km for the radius. The successful detection of Chiron later performed by Altenhoff & Stumpff (1995) at 1200 μm led to a radius of 84 km.

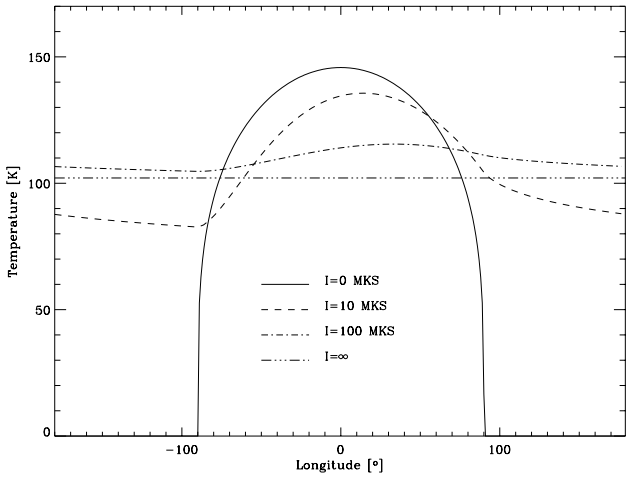

Fig. 3. Equatorial temperature profiles over the nucleus surface for thermal inertia I = 0, 10, 100 J K^{-1} m^{-2} s$^{-1/2}$ and ∞ at r = 8.5 AU.

2.3. Determinations of the radius and geometric albedo of the nucleus

The past infrared and radio observations were interpreted using either a standard thermal model (STM) which assumes no thermal inertia, or an isothermal-latitude model (ILM) which assumes an infinite thermal inertia (Lebofsky & Spencer 1989), or a modified STM which includes thermal inertia (Jewitt & Luu 1992). The strong influence of the thermal inertia I is highlighted in Fig. 3 where the surface temperature at the equator is plotted as a function of longitude. When I increases, the profile becomes smoother as more energy is transfered by conduction from the day side into the nucleus to heat the night side. In other words, when I increases, the temperature decreases on the day side and increases on the night side. In the extreme case of an infinite thermal inertia, the temperature is constant across the nucleus for a given latitude. Note that Chiron was always observed with a phase angle $\leq 7°$.

When using the infrared or radio observations alone, the size of the nucleus is determined assuming a geometric albedo. Adding visible observations allows to independently determine the size and the geometric albedo. This method, extensively used on asteroids, can give excellent results as recently demonstrated for 433 Eros: the combination of the visible and infrared ground-based observations performed in 1974/75 by Morrison (1976) led to a radius of 22 km and a geometric albedo of 0.18, a result in very good agreement with the recent in-situ observations performed by the NEAR spacecraft which led to a 33×13×13 km nucleus and a geometric albedo of 0.16. Table 3 summarizes the radius and geometric albedo determinations obtained by different authors for Chiron. Depending upon the observation and the model, the values vary from 71 km to 104 km with a mean value of ~88 km. Values of the geometric albedo range from 0.10 to 0.17, with a mean value of ~0.14.

Table 3. Radius and geometric albedo determination of Chiron.

Reference	r_n^a [km]	λ^b [μm]	Method	p_v^c	H_v^c
Lebofsky et al. (1984)	90^{+20}_{-25}	22.5	STM	$0.10^{+0.09}_{-0.035}$	6.9
Campins et al. (1994)	74 ± 11	19.2	STM	$0.14^{+0.06}_{-0.03}$	6.9
Campins et al. (1994)	88 ± 10	10.8	STM	–	–
Campins et al. (1994)	104 ± 10	19.2	STM	–	–
Campins et al. (1994)	94 ± 6	10.6	STM	–	–
Campins et al. (1994)	91 ± 13	20.0	STM	–	–
Fernandez et al. (2002)	74 ± 4	12.5, 17.9	STM	0.17 ± 0.02	6.96
Sykes & Walker (1991)	<186	60	ILM	>0.027	6.7
This work	71 ± 5	25, 60 and 100	MM + Conduction	0.11 ± 0.02	7.28
Jewitt & Luu (1992)	<150	800	STM + Conduction	>0.04	6.8
Altenhoff & Stumpff (1995)	84 ± 10	1200	STM	0.13	6.7
Buie et al. (1993)	>83		Occultation		
Bus et al. (1996)	89.6 ± 6.8		Occultation		
Bus et al. (1996)	>90.2 ± 6.5		Occultation		

[a] Nucleus radius. [b] Wavelength. [c] Derived geometric albedo. [d] Absolute V magnitude used for the geometric albedo determination.

The determination of the radius and the geometric albedo of the nucleus of Chiron faces two kinds of difficulties. First, it is model-dependent as a thermal model is required to interpret the infrared and radio observations. It is important to assess this dependence and, in particular, the impact of the thermal inertia. Second, the nucleus is often active and its coma, even too faint to be detected, may affect the results.

2.4. Occultation

The occultation of a star by a solid body is in principle a powerful method to determine its size. Such an event took place for Chiron in November 1993 and observations were attempted from five different sites in California. Only one site was successful in recording a useful lightcurve, although a second site had a marginal detection of the extinction of the starlight, and a preliminary value of the size of Chiron was reported by Buie et al. (1993). There are many problems involved in the analysis of an occulation, amplified in this case by the very small apparent size of Chiron (~0.03 arcsec) and by the presence of a coma. Moreover the sampling of the lightcurve is somewhat sparse, only eight points, and its interpretation is not unique, especially if a coma is introduced. The detailed analysis performed by Bus et al. (1996) led to two slightly different values (Table 3) depending upon whether the marginal detection is considered. Their analysis convincingly shows that the star track was nearly diametral and that a dust coma was indeed present (and possibly jets) consistent with an absolute magnitude $H_v = 6.41$ at the time of the occultation. Taking into account the marginal detection, they determined a radius of 89.6 ± 6.8 km.

3. Nucleus thermal model

3.1. General considerations

In order to interpret the ISOPHOT observations as well as all other thermal observations in a coherent way, we considered a thermal model as well as appropriate assumptions. We assumed a spherical nucleus rotating with a period of 5.92 h with its spin axis perpendicular to the comet orbital plane, in good agreement with the observations discussed in the previous section. The parameter Θ introduced by Spencer et al. (1989) is useful to estimate the influence of the heat conduction and to choose the appropriate thermal model. It is defined as:

$$\Theta = \frac{I\sqrt{\omega}}{\epsilon\sigma T_{ss}^3} \quad (2)$$

where I is the thermal inertia, ω is the rotational frequency, ϵ is the infrared emissivity, σ is the Stefan Boltmann's constant and T_{ss} is the subsolar equilibrium temperature. $\Theta \ll 1$ implies a slow-rotator and $\Theta \gg 1$, a fast-rotator. For Chiron, with a nucleus spin period $P_n = 5.92$ h and a maximum surface temperature T_{ss} of 150 K (Fig. 3), we obtained $\Theta \sim 1$ for a thermal inertia $I = 10$ MKS (where 1 MKS unit = 1 J K^{-1} m^{-2} s$^{-1/2}$) and $\Theta \sim 10$ for $I = 100$ MKS. Chiron is therefore intermediate between the slow and the fast-rotators and the heat conduction into the nucleus must be introduced. We consider a mixed model of refractory dust and water ice grains in an attempt to take into account the detection of water ice on the surface of Chiron (Foster et al. 1999; Luu et al. 2000). Our model does not take into account the sublimation of CO as we assumed that CO is located deep below the surface so that its effects on the surface temperature are negligible.

3.2. The mixed model (MM)

The mixed model (MM) has already been introduced by Lamy et al. (2002) to interpret the infrared observations of the nucleus of 22P/Kopff. It assumes an intimate, microscopic mixture of dust and water ice grains, so that the thermal coupling between the grains is perfect and there is only one temperature for the mixture. As the ice is "dirty", the geometric albedo can be low (Clark & Lucey 1984) and this is further discussed in Sect. 4.2 below. As explained by Jewitt & Luu (1992), the sublimation of water ice can be neglected for Chiron, and in this case, our MM is equivalent to their thermal model: a STM with heat conduction. Thermal balance on the surface between the solar flux received by the nucleus on the one hand, the reradiated flux and the heat conduction on the other hand is expressed as:

$$(1-A)\frac{F_{\rm sun}}{r_{\rm h}^2}\cos z = \eta\epsilon\sigma T^4 + \kappa\left.\frac{\partial T}{\partial x}\right|_{x=0} \quad (3)$$

where $A = p_v q$ is the product of the geometric albedo p_v with the phase integral q, $F_{\rm sun}$ [Wm^{-2}] is the solar constant, $r_{\rm h}$ [AU] is the heliocentric distance, z is the zenithal angle, η is the beaming factor introduced by Lebofsky & Spencer (1989), T [K] is the surface temperature, κ [Wm^{-1}K^{-1}] is the thermal conductivity and x measures the depth. Numerical values for the parameters will be discussed in Sect. 3.4. Although the sublimation of water ice is neglected, its presence on the surface will appear through the Bond albedo A.

We considered the one-dimensional time-dependent equation for the heat conduction:

$$\rho C\frac{\partial T(x,t)}{\partial t} = \frac{\partial}{\partial x}\left(\kappa\frac{\partial T(x,t)}{\partial x}\right) \quad (4)$$

where ρ [kg/m^3] is the mass density and C [J/kg/K] is the specific heat capacity of the nucleus. We solved this equation using a method similar to that described by Spencer et al. (1989). We changed x to $x' = x/\xi$, where $\xi = \sqrt{2\kappa/\rho C\omega}$ [m] is the characteristic length of the heat wave which propagates into the subsurface. Then, Eq. (4) becomes Eq. (5) and Eq. (3) becomes Eq. (6):

$$\frac{\partial T(x',t)}{\partial t} = \frac{\omega}{2}\frac{\partial^2 T(x',t)}{\partial x'^2} \quad (5)$$

$$(1-A)\frac{F_{\rm sun}(t)}{r_{\rm h}^2}\cos z = \eta\epsilon\sigma T^4(0,t) + \sqrt{\frac{\omega}{2}}\sqrt{\kappa\rho C}\frac{\partial T(0,t)}{\partial x'} \quad (6)$$

where $\omega = 2\pi/P_{\rm n}$ is the rotational frequency.

The boundary conditions are given by Eq. (6) at the surface, and by Eq. (7) at a depth d:

$$\left(\frac{\partial T(x,t)}{\partial x}\right)_{x=d=12\xi} = 0 \quad \text{or} \quad \left(\frac{\partial T(x',t)}{\partial x'}\right)_{x'=12} = 0. \quad (7)$$

This last condition assumes that the temperature remains constant below a (thick enough) layer of thickness d. The choice of this constant temperature is explained in detail by Spencer et al. (1989). We took $d = 12\xi$, which ensures a good convergence; a higher d does not change the surface temperature.

Table 4. Estimated thermal inertia I for different bodies of the Solar System.

Body	I [J K^{-1} m^{-2} s$^{-1/2}$]	Reference
Moon	50	Winter & Saari (1969)
Mars	65−460	Kieffer et al. (1977)
Phobos	37−67	Lunine et al. (1982)
Deimos	28−84	Lunine et al. (1982)
Saturn rings	13	Froidevaux et al. (1981)
Eros	<105	Morrison (1976)
Ganymede	84−167	Morrison et al. (1971)
Asbolus	<10	Fernandez et al. (2002)
1P/Halley	<670	Julian et al. (2000)

In Eq. (6), all thermal parameters of the nucleus are regrouped into a single quantity, the thermal inertia $I = \sqrt{\kappa\rho C}$ [J K^{-1} m^{-2} s$^{-1/2}$]. This is now the only parameter that we will consider when solving the system of Eqs. (5)+(6)+(7). Table 4 gives estimates of the thermal inertia for different bodies of the Solar System.

The nucleus is divided in several layers of thickness dx' where d$x' = 0.25$ is enough for Chiron to ensure a good convergence. The longitude is represented by the time parameter t. As t increases, the nucleus rotates and the longitude, reckoned from the sub-solar point, changes. We took a step d$t = P_{\rm n}/1000$, which correponds to ~21 s for a period $P_{\rm n} = 5.92$ h and which is enough to reach the convergence. Tests were performed with lower values of dx' and dt and led to marginal differences.

We calculated the temperature T at each point (θ, φ) of the surface to obtain a temperature map $T(\theta, \varphi)$, where θ is the latitude and φ is the longitude. For illustration, the temperature profile along the equator ($\theta = 0°$) is displayed in Fig. 3 for different thermal inertia.

3.3. The thermal flux

The thermal flux $F(\lambda)$ of an unresolved nucleus measured by an observer located at geocentric distance Δ is the integral over the nucleus of $\epsilon B(\lambda, T)$ where $B(\lambda, T)$ is the Planck function and $T(\theta, \varphi, A)$ is given by the MM:

$$F(\lambda) = \epsilon\int\int B\left[\lambda, T(\theta,\varphi,A)\right]\Omega {\rm d}S. \quad (8)$$

The solid angle Ω is given by:

$$\Omega = \frac{1}{\Delta^2}\cos\theta\cos(\varphi-\alpha) \quad (9)$$

and the element of surface by:

$${\rm d}S = r_{\rm n}^2\cos\theta{\rm d}\theta{\rm d}\varphi \quad (10)$$

where $r_{\rm n}$ is the radius of the nucleus, θ is the latitude, φ is the longitude measured from the sub-solar point and α is the phase angle. θ and φ are linked to the zenithal angle z by $\cos z = \cos\theta\cos\varphi$. We calculated the thermal flux by performing a double integration over the hemisphere of the nucleus which is visible from Earth i.e., satifying $\cos(\varphi-\alpha) > 0$.

3.4. The model parameters

The various parameters involved in the thermal models are not known for cometary nuclei. We discuss below how we selected their respective values.

The infrared emissivity ϵ is taken equal to 0.95, the middle point of the interval 0.9−1.0 always quoted in the literature. As the interval is very small and the value near 1.0, this uncertainty has a negligible influence on the calculated thermal flux.

The beaming factor η reflects the influence of surface roughness which produces an anisotropic thermal emission, and theorically ranges from 0 to 1. For physical reasons, η is higher than 0.7, otherwise it implies a very high, unrealistic, roughness, with a rms slope higher than 1 (Lagerros 1998). We adopted the value of $\eta = 0.756$, derived from observations of 1 Ceres and 2 Pallas by Lebofsky et al. (1986), as those objects have a geometric albedo (0.10 and 0.14 respectively) similar to that of Chiron. Note that, on the basis of the work of Lagerros (1998), Lamy et al. (2002) used a slightly larger value $\eta = 0.85$ for the nucleus of 22P/Kopff as this body has a lower geometric albedo $p_v = 0.04$. As the temperature varies as $\eta^{-1/4}$, the beaming factor may have an important effect on thermal flux and, in turn, on the radius determination of the nucleus.

The Bond albedo A requires a knowledge of the phase integral q, which measures the angular dependence of the scattered radiation. We choose $q = 0.4$, the value found for 2 Pallas (Lebofsky et al. 1986) since its geometric albedo $p_v = 0.14$ is comparable to that of Chiron. We note that this value of q is significantly different from the value $q = 0.28$ chosen for 22P/Kopff (Lamy et al. 2002) since those two objects have quite difference surface properties. However q has little influence and the above values yielded similar results.

For the geometric albedo, we took $p_v = 0.11$, which is the value derived from the ISOPHOT observations and which will be discussed in the next section. It will then be shown that the results are almost independent of the geometric albedo in the range 0.01−0.15.

4. Results and discussion

4.1. Thermal inertia and radius determination of the nucleus

The determination of the thermal inertia I and the radius r_n of the nucleus is performed by minimizing the χ^2 expression defined as:

$$\chi^2(I, r_n) = \sum_{i=1}^{n} \left[\frac{F_i - F(\lambda_i, I, r_n)}{\sigma_i} \right]^2 \quad (11)$$

where F_i is the measured flux at the wavelength λ_i and σ_i the corresponding error bar. We took into account the average ISOPHOT fluxes from the three nights of observation presented in Sect. 2.2 (Table 2), at 25, 60 and 100 μm. We did not take into account the observation at 160 μm in our discussion for reasons explained in Sect. 2.2. Figure 4 presents the value of χ^2 as a function of I and r_n. Its lower value is obtained, at the 1 σ level ($\chi^2 < 1$), for a radius $r_n = 71 \pm 5$ km and a thermal inertia $I = 3^{+5}_{-3}$ MKS.

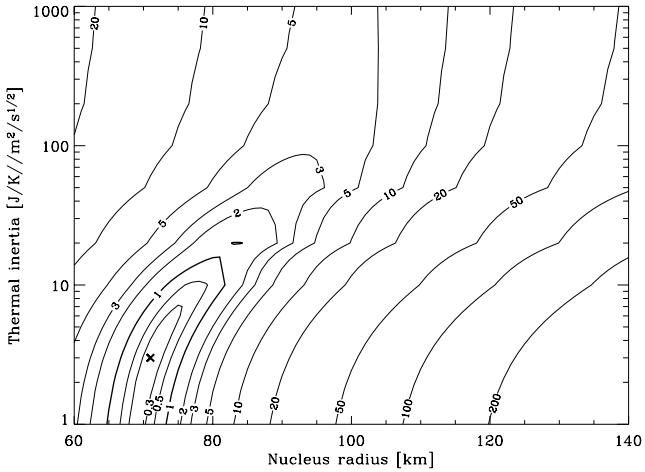

Fig. 4. Value of the χ^2 expression as a function of the radius r_n and the thermal inertia I. The cross represents best estimate of r_n and I, i.e. where χ^2 is minimum.

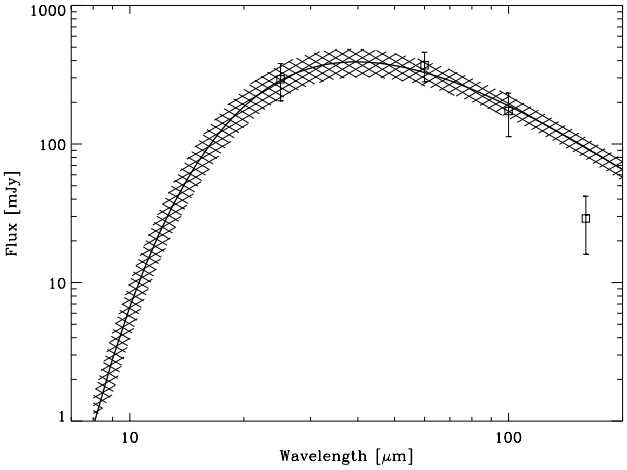

Fig. 5. The SED of the nucleus of Chiron for the mixed model (MM) with a radius $r_n = 71 \pm 5$ km and a thermal inertia $I = 3^{+5}_{-3}$ MKS. The squares are the ISOPHOT data at 25, 60, 100 and 160 μm with their 1σ error bars.

Figure 5 displays the SED of Chiron from 10 μm to 200 μm for the mixed model (MM), for the above values and the 1 σ uncertainty. The fit to the data points is excellent, except at 160 μm for reasons already discussed.

The value of 71 ± 5 km for the radius is lower than the bulk of the previous estimates (Table 3), but in excellent agreement with the recent determination of 74 ± 4 km by Fernandez et al. (2002). The value of 3^{+5}_{-3} MKS for the thermal inertia is very low, but coherent with our present understanding of primitive bodies. Indeed, Fernandez et al. (2002) determined a thermal inertia <10.5 MKS for Asbolus, and Spencer et al. (1989) suggested a thermal inertia <15 MKS for asteroids Ceres and Pallas, lower than that of the Moon (50 MKS). The low thermal inertia of Chiron indicates a low thermal conductivity for the surface material, and probably a porous surface as supposed for the majority of cometary nuclei (e.g. Klinger et al. 1996; Skorov et al. 1999).

As pointed out above, the only parameter on which the thermal model and consequently the results are sensitive is the

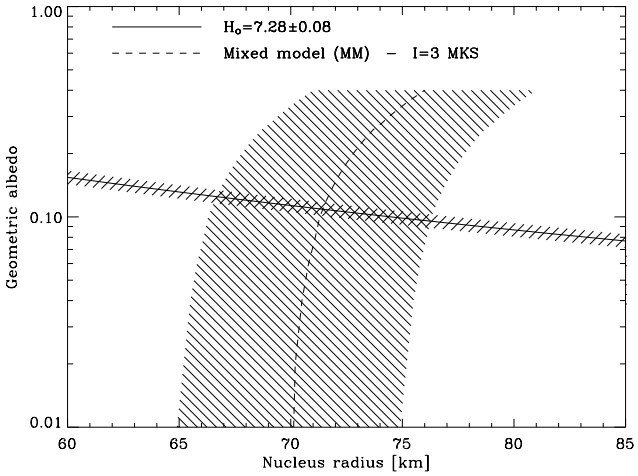

Fig. 6. The albedo-radius diagram for Chiron. The infrared constraints come from the ISOPHOT observations with the models presented in Fig. 3. The visible constraint is given by the visible absolute magnitude of the nucleus of Chiron $H_0 = 7.28 \pm 0.08$.

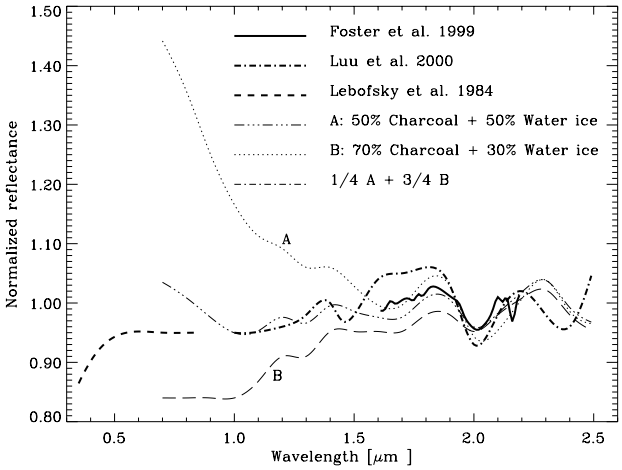

Fig. 7. Observed spectra of Chiron compared to laboratory experiments with mixtures of charcoal and water ice.

beaming factor η, which ranges from 0.7−1.0 (see Sect. 3.4). For $\eta = 0.756$, as justified in Sect. 3.4, we obtained the best fit with a radius $r_n = 71$ km and a thermal inertia $I = 3$ MKS. For the extreme, unrealistic value of $\eta = 1.0$, the best fit is obtained with $r_n = 77$ km and $I = 0$ MKS, and for $\eta = 0.7$ with $r_n = 71$ km and $I = 5$ MKS. For $\eta = 0.85$, the value used for 22P/Kopff (Lamy et al. 2002), we obtained $r_n = 72$ km and $I = 0$ MKS. Consequently, the choice of η, in the range 0.7−0.85, has practically no influence on the determination of the radius and the thermal inertia.

4.2. Geometric albedo

In order to determine the size and the geometric albedo of Chiron without any assumptions, we need two independent relationships. The first one is given by the visible observations and we used the value discussed in Sect. 2.1, $H_0 = 7.28 \pm 0.08$, for the absolute V magnitude of the nucleus. The nucleus radius r_n and the geometric albedo p_v are linked to H_0 using the relationship of Bowell et al. (1989):

$$\log(2r_n) = 3.130 - 0.2H_0 - 0.5 \log p_v. \quad (12)$$

The second relationship between r_n and p_v is given by the thermal flux via Eq. (8) where the surface temperature T depends on p_v through $A = p_v q$. We used $I = 3$ MKS, as determined previously, and the ISOPHOT fluxes at 25, 60 and 100 μm. We graphically combined the visible and the infrared constraints, as illustrated in Fig. 6. The curves represents the infrared and visible constraints which cross themselves nearly orthogonally; this minimizes the error on the determination of r_n and p_v. Moreover, the infrared constraint is almost independent of the geometric albedo in the range 0.01−0.15, yielding a quasi constant value for the radius in this range (variation <3%). The geometric albedo is only constrained by the absolute magnitude of the nucleus H_0.

For our solution, a MM with a thermal inertia of 3 MKS and a radius of 71 km, we obtained a geometric albedo of 0.11 ± 0.02, the uncertainty coming from the error affecting H_0. This value is in excellent agreement with the determination of Campins et al. (1994). Fernandez et al. (2002) obtained a higher geometric albedo of 0.17 ± 0.02 assuming $H_0 = 6.96$. Using $H_0 = 7.28$ instead yields 0.13 ± 0.02, in excellent agreeement with our determination. The geometric albedo cannot be used to constrain the thermal inertia. This shows the importance of combining infrared AND visible observations to estimate altogether p_v, r_n and I.

The geometric albedo of 0.11 is higher than the typical range 0.02−0.06 found for the nucleus of short period comets (Lamy et al. 2004) and this probably results from the presence of water ice at the surface of Chiron, a question discussed in the following section.

4.3. Reflectance of Chiron

We now consider the spectrum of Chiron to characterize its surface. We assembled a composite spectrum by combining the results of Lebofsky et al. (1984), Foster et al. (1999) and Luu et al. (2000) in Figs. 7–10. We normalized the spectrum of Foster et al. and Luu et al. at 2.2 μm, and we applied a scaling factor of 0.95 to the spectrum of Lebofsky et al. (originally normalized at 0.55 μm) in order to insure continuity at 1 μm. Each spectrum was sampled and then interpolated using cubic splines. There are obvious problems with the infrared spectra, in particular with that of Luu et al. (2000): the 1.5 μm band appears misplaced and the apparent absorption longward of 2.2 μm is probably spurious. However, the composite spectrum exhibit well-defined features, an almost flat part extending from 0.5 to 1.1 μm and the two aborption band of water ice at 1.5 and 2.0 μm. These features, and particulary the contrast of the bands, can be used to set limits on the fractional coverage of ice.

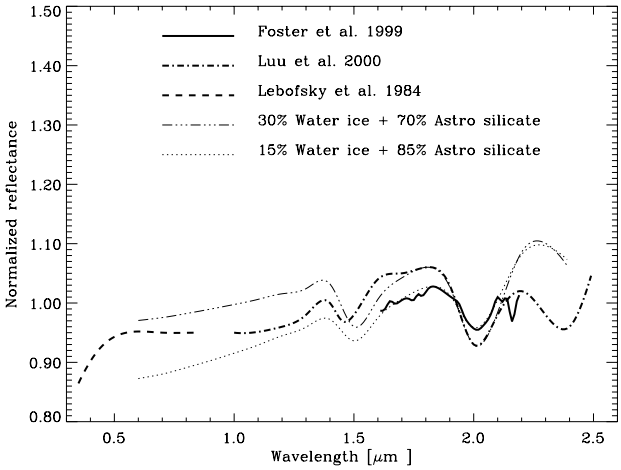

Fig. 8. Observed spectra of Chiron compared to two mixtures of astronomical silicate and water ice grains in different proportions. The grain size is 10 μm.

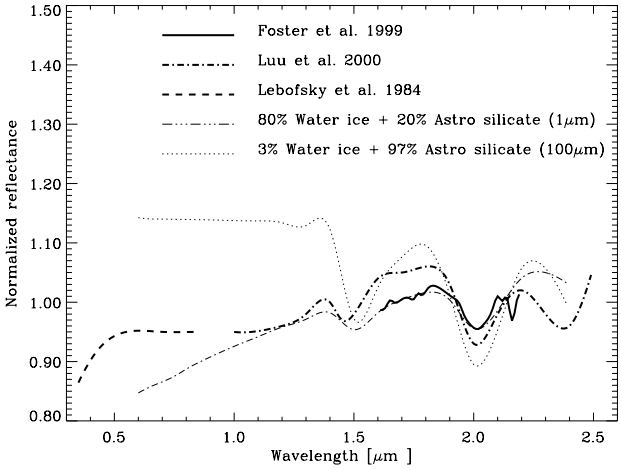

Fig. 9. Observed spectra of Chiron compared to two mixtures of astronomical silicate and water ice grains, with grain sizes of 1 and 100 μm.

4.3.1. Comparison with experimental spectra from laboratory experiments of microscopic mixtures

We start by comparing the spectrum of Chiron with laboratory results on different samples which are intimate, microscopic mixtures of different grains. The main advantage of using spectra obtained with laboratory experiments is that they are far more realistic than computed spectrum, which further involve many unknown parameters. Figure 7 diplays the reflectance of two mixtures of water ice and charcoal measured by Clark & Lucey (1984) using the experiment chamber of Clark (1981). Mixture A (50% charcoal +50% water ice) exhibits a 2.0 μm band approximately similar to the observed one but unfortunately a steep gradient in the visible. Mixture B (70% charcoal +30% water ice) alleviates this problem at the expense of producing too low a reflectance in the visible and too low a contrast of the 2.0 μm band. None of the two mixtures exhibits the 1.5 μm aborption band. It is tempting to use a linear combination of the A and B spectra to better reproduce the observations. Figure 7 displays the solution "0.25 A + 0.75 B" which indeed

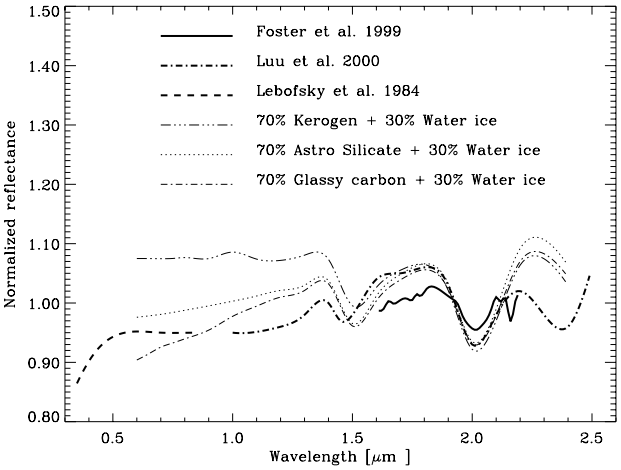

Fig. 10. Observed spectra of Chiron compared to three different mixtures of 30% of water ice +70% of refractory grains (silicate, glassy carbon or kerogen). The grain size is 10 μm.

offers a better fit to the observations than any of the two individual mixtures. Applying the above linear scaling, this solution contains approximately 65% of charcoal and 35% of water ice. The fit is not perfect but gives a rough idea of the amount of water ice on the surface of Chiron, ~35%. Unfortunately, the geometric albedo of a body having a surface composed of such a mixture is not known but is probably low owing to the large percentage of refractory material, a result justified in the next section.

4.3.2. Comparison with computed spectra of macroscopic mixtures

We now calculate the reflectance of simple areal mixtures of water ice and other refractory materials. The advantage of this approach is twofold, first the parameters may be varied at will, and second the reflectance *and* the geometric albedo of a body covered with the considered mixture can be simultaneously calculated. The drawback of this approach is the large number of (unknown) parameters such as the optical properties of the materials and the distribution function of the grain size, and the solutions are no means unique. The model considers macroscopic mixtures so that there is no interaction between the components, and the resulting reflectance spectrum is a linear combination of the individual spectra according to the selected fractional coverage of each component. It has already been applied to Chiron: Foster et al. (1999) combined 20% of water ice with 80% of a spectrally neutral material while Luu et al. (2000) combined water ice and olivine in unspecified proportion to interpret their observations.

For the present study, we used the numerical code of Roush (1994), based on the Hapke formalism (Hapke 1993) and considered mixtures of water ice with three different refractory materials. First, a silicate, known as "astronomical silicate" in the literature; its optical constants come from Draine & Lee (1984). Second, glassy carbon, an amorphous form of carbon; its optical constants come from Edoh (1983). Third, a kerogen, a highly processed organic residue; its optical constants come

Table 5. Calculated geometric albedos for different mixtures of water ice + astronomical silicates and different grain sizes.

Mixture[a]	Grain size [μm]	Albedo[b]
3%	100	0.02
15%	10	0.06
30%	10	0.11
80%	1	0.33

[a] Percentage of water ice in the mixture water ice + astronomical silicates. [b] Geometric albedo.

from Khare et al. (1990). The optical constants of water ice come from Warren (1984).

Figure 8 displays our results obtained for a mixture of water ice + silicate with a unique grain size of 10 μm. The percentage of water ice was tuned to produce the observed contrast of the 2.0 μm band. It amounts to 15% to match the spectrum of Foster et al. (1999) and to 30% to match that of Luu et al. (2000). The fits are quite satisfactory in the interval 1.4 to 2.1 μm in spite of a slight mismatch of the 1.5 μm band, but this may comes from the spectrum of Luu et al. (2000) as discussed above. However, the amount of water ice strongly depends upon the grain size. Figure 9 displays the same fit but, for two different grain sizes, 1 μm and 100 μm. In order to match the observed spectrum and especially the contrast of the 2.0 μm band, the amount of water ice must be less than 3% for a grain size of 100 μm, and larger than 80% for a grain size of 1 μm.

In order to test whether the above mixtures are compatible with the albedo of 0.11 ± 0.02 determined in Sect. 4.2, we used a numerical code written by Roush (1994) to calculate the geometric albedo of a spherical body in the framework of the Hapke formalism. The results for the four mixtures water ice + astronomical silicate considered in Figs. 8 and 9 are represented in Table 5. We obtained similar results for the other refractory materials, glassy carbon and kerogen. The solution which best matches both the observed reflectance and albedo of Chiron corresponds to a mixture of 30% of water ice +70% of refractory material and a common grain size of ∼10 μm. The resulting spectra are displayed in Fig. 10. Smaller grain sizes would require larger water ice fractions resulting in very large albedos while larger grain sizes result in the opposite situation. None of the mixture exhibits the observed visible spectrum of Chiron althougth the discrepancies are not that large and much reduced compared to the previous solution (Fig. 7). One cannot reasonably hope that any of the selected material precisely corresponds to the refractory component of Chiron. For the three cases of surface composition introduced above (Fig. 10), we found geometric albedos of respectively 0.11 (silicate), 0.13 (glassy carbon) and 0.10 (kerogen), all in excellent agreement with our result of 0.11 ± 0.02.

In summary, the spectrum of the nucleus of Chiron and its relatively high geometric albedo are both consistent with a surface approximately composed of 30% of water ice and 70% of a refractory material.

Table 6. Nucleus radius from IR and radio observations of Chiron.

Date[a]	Reference	λ [μm]	Radius[b] [km]
09 Jan. 1983	Lebofsky et al. (1984)	22.5	97 ± 30
18 Nov. 1991	Campins et al. (1994)	19.2	79 ± 15
22 Nov. 1993	Campins et al. (1994)	10.8	102 ± 14
	Campins et al. (1994)	19.2	114 ± 12
31 Mar. 1994	Campins et al. (1994)	10.6	112 ± 9
	Campins et al. (1994)	20.0	98 ± 16
21 Jun. 2000	Fernandez et al. (2002)	12.5	87 ± 6
	Fernandez et al. (2002)	12.5	98 ± 8
23 Jun. 2000	Fernandez et al. (2002)	12.5	87 ± 6
	Fernandez et al. (2002)	17.9	62 ± 12
	Fernandez et al. (2002)	17.9	70 ± 11
16 Sep. 1983	Sykes & Walker (1991)	25	<164
	Sykes & Walker (1991)	60	<127
Jun. 1996	This work	25	71 ± 6
	This work	60	75 ± 12
	This work	100	67 ± 14
22 Mar. 1991	Jewitt & Luu (1992)	800	<138
27 Apr. 1994	Altenhoff & Stumpff (1995)	1200	74 ± 9

[a] See Table 2 for observation conditions. [b] Radius derived from the mixed model (MM) with a thermal inertia $I = 3$ J K^{-1} m^{-2} s$^{-1/2}$.

4.4. Comparison with previous infrared and radio observations

We now systematically apply our thermal model, i.e., the mixed model with the parameters given in Sect. 3.4, a geometric albedo of 0.11 and a thermal inertia of 3 MKS, to all past infrared and radio observations. This is the first time that this set of observations is homogeneously analyzed with the same model, thus allowing a meaningful comparison of the resulting sizes of the nucleus of Chiron. Table 6 summarizes the different radius determinations which may differ from those found by the authors (cf. Table 3) since they used different thermal models and/or different parameters. Figure 11 displays the radius determination versus wavelength for all observations listed in Table 6. Our result $r_n = 71 \pm 5$ km given by our mixed model is in excellent agreement with all observations above 20 μm, including the submillimetric observations of Altenhoff & Stumpff (1995) at 1200 μm. Our result is also consistent with the observations of Fernandez et al. (2002) at 17.9 μm and one observation of Campins et al. (1994) at 19 μm. The other observations of Campins et al. (1994) tend to suggest a larger radius. This trend is more pronounced at ∼10 μm, and the observations of Campins et al. (1994) and Fernandez et al. (2002) yield a radius of 87−112 km. A radius of 71 ± 5 km is not compatible with the occultation performed by Bus et al. (1996), unless taking into account their error bars at the 3σ level. The question of reconciling thermal infrared observations with results from occultations has already been addressed by Fernandez et al. (2002).

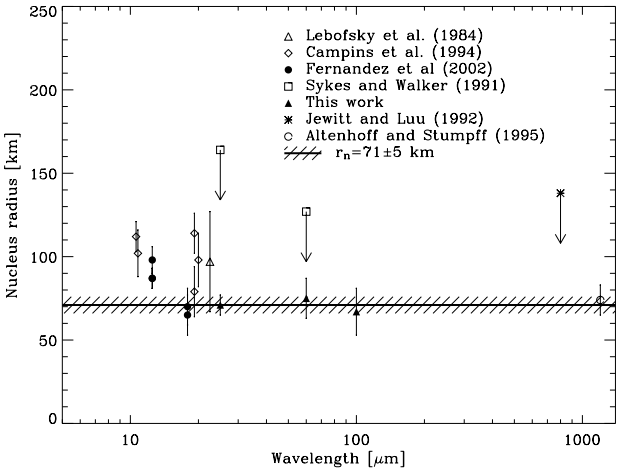

Fig. 11. Determination of the radius of Chiron from the infrared and radio observations of Table 2, using a mixed model (MM) with a geometric albedo of 0.11 and a thermal inertia of 3 MKS. The solid bold line and the hatched band represent our determination of 71 ± 5 km.

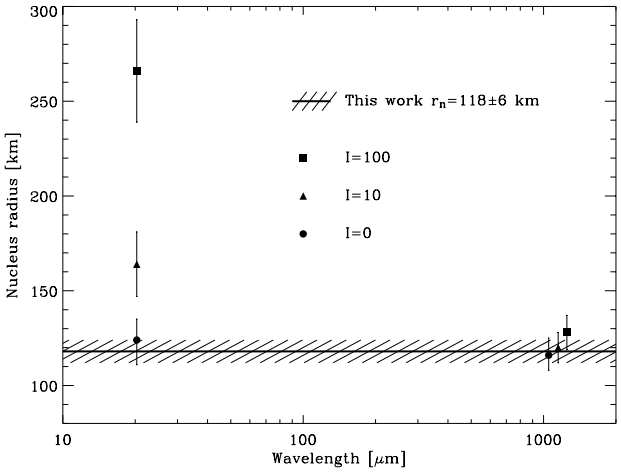

Fig. 12. Determination of the radius of Chariklo from the 20.3 μm infrared and 1.2 mm radio observations of Table 7. Differents symbols are used for I = 0, 10 and 100 MKS. The symbols at 1.2 mm have been deliberately offset left-right for clarity. The solid bold line and the hatched band represent our determination of 118 ± 6 km.

4.5. Coma contribution

We address the question of a possible contamination of the ISOPHOT observations by the coma by noting that our visible observation performed 10 days later (25 June 1996) yielded H_v = 6.57. Assuming an absolute V magnitude of the nucleus of 7.28, we derived a coma contribution of 48% using:

$$\frac{F(\text{obs.}) - F(\text{nucl.})}{F(\text{obs.})} = \frac{10^{-0.4\times6.57} - 10^{-0.4\times7.28}}{10^{-0.4\times6.57}} = 48\%. \quad (13)$$

But, since we derived a radius of 71 km, lower than previous determinations, it is very unlikely that there was any significant contribution of the coma to the infrared fluxes (if present at all, a faint coma contribution would be hidden by the large uncertainty of ~30% affecting the measurements). This has already been pointed out by Campins et al. (1994), two years before the ISOPHOT observations, when Chiron was even more active, and by West (1991), who argued that the blue color of the coma is most likely due to scattering by submicron dust grains.

5. Application to the Centaur Chariklo

5.1. Radius, thermal inertia and geometric albedo of the nucleus

Chariklo (1997 CU26) was discovered in 1997 with the Spacewatch telescope (Scotti 1997). It has a perihelion of 13.07 AU, an aphelion of 18.35 AU, an excentricity of 0.31 and an inclination of 30.1°, which classifies it in the Centaur family. Several observations were attempted in order to characterize its physical properties. The visible observations of Davies et al. (1998) gave an absolute V magnitude H_v = 6.82 ± 0.02, using a linear phase function with β = 0.05 mag deg^{-1}. Combining this result with the infrared flux obtained at 20.3 μm, Jewitt & Kalas (1998) derived a radius of 151 km and a geometric albedo of 0.045. Altenhoff et al. (2001) performed radio observations at 1.2 mm and determined a radius of 137 km and a geometric albedo of 0.055. The infrared and radio observations

Table 7. Infrared and radio observations of Chariklo.

Date	r_h^a [AU]	Δ^b [AU]	α^c [°]	λ^d [μm]	Flux [mJy]	Ref.
13 Jan. 1998	12.81	13.72	1.7	20.3	66^{+14}_{-11}	(1)
Dec. 99-Feb. 00	13.35	12.62	3.0	1200	2.08 ± 0.30	(2)

[a] Heliocentric distance. [b] Geocentric distance. [c] Phase angle in degrees. [d] Wavelength.
References: (1) Jewitt & Kalas (1998); (2) Altenhoff et al. (2001).

are presented in Table 7. The recent observations of Peixinho et al. (2001) present evidences for variations of the absolute magnitude of Chariklo over a few months. Using these data with a linear phase function correction (β = 0.05 mag deg^{-1}), we determined a range for H_v from 6.52 to 6.90, well within the error bars. We applied our model used for Chiron to those visible, infrared and radio observations, in order to determine altogether the radius, the geometric albedo and the thermal inertia of Chariklo. We adopted a rotation period of 24 h (Davies et al. 1998).

As done for Chiron, we minimized the χ^2 expression, using the infrared (Jewitt & Kalas 1998) and radio (Altenhoff et al. 2001) constraints, and we derived a radius of 118 ± 6 km and a thermal inertia of 0^{+2}_{-0} MKS. As noted previously, this results depend on η. For η in the range 0.7−1.0, the χ^2 expression is minimum for a radius in the range 115−126 km and a thermal inertia of 0 MKS. Consequently, the influence of η is null on the thermal inertia and <10% on the radius. For Chariklo, I must be less than 2 MKS, otherwise the infrared and radio observations are not compatible. This is illustrated in Fig. 12, where we represented the radius determination for different thermal inertia in the range 0−100 MKS, as a function of wavelength. The infrared observations lead to a range of radius of 124 to 266 km, while the radio observations lead to a much narrower range of 116 to 128 km, thus giving a stringent constraint on the

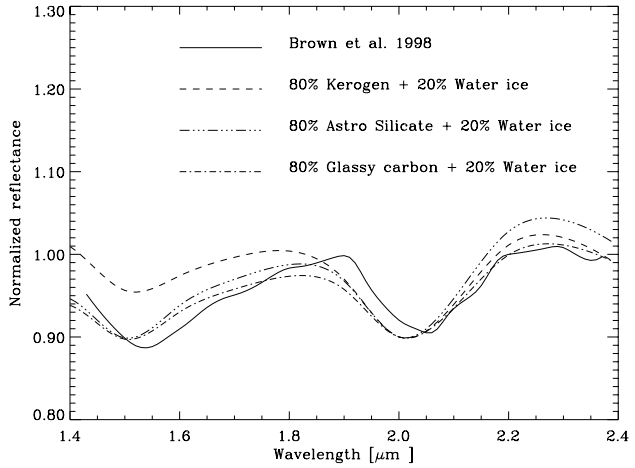

Fig. 13. The observed spectrum of Chariklo compared to four different mixtures of water ice and refractory grains (silicate, glassy carbon or kerogen). The grain size is 10 μm.

nucleus. This large difference of range between the two spectral domains has already been addressed (Sect. 2.2). Using Eq. (12) with the values of $r_n = 118 \pm 6$ km and $H_0 = 6.70 \pm 0.20$, we derived a geometric albedo of 0.07 ± 0.01.

5.2. Reflectance of Chariklo

In order to complete the analysis of Chariklo, we considered its reflectance using the spectrum obtained by Brown et al. (1998), which we normalized at 2.2 μm. We favored this spectrum over that obtained more recently by Brown (2000) as this latter is of lower quality. Likewise that of Chiron, it exhibits the water ice absorption bands at 1.5 and 2.0 μm with approximatively the same contrast (compare Figs. 13 and 10). We know from Sect. 5.1 that the geometric albedo of Chariklo (0.07 ± 0.01) is slightly lower than that of Chiron (0.11 ± 0.02), and this requires that the fractional coverage of ice be reduced in comparison to that of Chiron. In view of the previous discussion in Sect. 4.3.2, we adopted a grain size of 10 μm and found that the solution which best matches the observed spectrum is composed of 20% of water ice +80% of refractory materials (either kerogen, silicate or glassy carbon). As illustrated in Fig. 13, these mixtures give excellent fits to the spectrum of Chariklo. The corresponding geometric albedos are 0.07 (silicate), 0.09 (glassy carbon) and 0.07 (kerogen), in good agreement with the above determination of 0.07 ± 0.01.

In summary, the spectrum of the nucleus of Chariklo and its geometric albedo of 0.07 ± 0.01 are both consistent with a surface approximately composed of 20% of water ice and 80% of a refractory material.

6. Conclusion

We have analyzed visible, infrared, radio and spectroscopic observations of 2060 Chiron and 1997 CU26 Chariklo in a synthetic way to determine the physical properties of its nucleus. Our main results are summarized below:

1. The analysis of the visible observations performed from September 1969 to August 2001 leads to an absolute V magnitude for the nucleus of Chiron $H_0 = 7.28 \pm 0.08$ with a lightcurve amplitude of 0.16 ± 0.03 mag, implying a nearly spherical nucleus with a ratio of semi-axes $a/b = 1.16 \pm 0.03$.
2. The analysis of the infrared ISOPHOT observations of Chiron, which covers the maximum of the SED (25, 60 and 100 μm), with a thermal model which includes heat conduction leads to a thermal inertia of 3^{+5}_{-3} J K^{-1} m^{-2} s$^{-1/2}$ and a radius of 71 ± 5 km. Combining the visible and infrared observations, we found a geometric albedo of 0.11 ± 0.02. This solution is remarkably consistent with observations ranging from 17.9 μm (Fernandez et al. 2002) to 1200 μm (Altenhoff et al. 1995).
3. This very low value of the thermal inertia, the lowest ever determined for a body of the Solar System, is supported by other evidences and is coherent with our present understanding of primitive bodies. It implies a low thermal conductivity and probably a porous structure as often assumed for cometary nuclei.
4. The spectrum of the nucleus of Chiron and its relatively high geometric albedo are both consistent with a surface composed of a mixture of water ice (~30%) and refractory (~70%) grains.
5. The same analysis for the visible, infrared and radio observations of Chariklo (1997 CU26), yields a radius of 118 ± 6 km, a geometric albedo of 0.07 ± 0.01 and a thermal inertia of 0^{+2}_{-0} J K^{-1} m^{-2} s$^{-1/2}$, making Chariklo the largest Centaur detected so far. A surface composed of a mixture of water ice (~20%) and refractory (~80%) grains is compatible with its near-infrared spectrum and the above albedo.

The wide diversity in the optical and near-infrared reflection spectra of Centaurs is now well established and can be interpreted in terms of different histories leading to mantles of different nature (Jewitt & Fernandez 2001). This is reinforced by the differences in albedo as illustrated by the two cases considered here, Chiron and Chariklo, which can be related to different properties (composition, porosity) of the uppermost layers of the two nuclei. Our results further suggest different thermal inertia for Chiron and Chariklo. It is tempting to relate this possible difference to the presence (Chiron) or absence (Chariklo) of activity, the larger heat conduction in Chiron implying that more energy reach the CO layer inside the nucleus thus producing its sublimation. This question is beyong the scope of the present study but would be worth exploring.

As Centaurs will eventually become ecliptic comets, it is quite interesting to compare the properties of these two families. A major difference is that water ice has been detected at the surface of several Centaurs on the basis of the 1.5 and 2.0 μm absorption bands, while it has never been detected on any ecliptic comet nucleus. From the few determinations presently available and clearly on the basis on the above results, several Centaurs have a geometric albedo distinctly larger than that of short period comets. Our calculation suggests that the large fraction of water ice present on the surface of these Centaurs also explain these large albedo values. This would indicate that sublimation is quite effective in weathering the cometary surfaces and decreasing their albedo.

Acknowledgements. We express our gratitude to T.L. Roush, who kindly made his program to calculate the reflectance and the geometric albedo available to us and for his helpful comments. We thank the referee, D.P. Cruikshank, for many helpful comments.

References

Altenhoff, W. J., & Stumpff, P. 1995, A&A, 293, L41
Altenhoff, W. J., Menten, K. M., & Bertoli, F. 2001, A&A, 366, L9
Bauer, J. M., Meech, K. J., Fernández, Y. R., et al. 2003, Icarus, in press
Bowell, E., Hapke, B., Domingue, D., et al. 1989, Asteroids II
Brown, R. H., Cruikshank, D. P., Pendleton, Y., & Veeder, G. J. 1998, Science, 280, 1430
Brown, M. E. 2000, AJ, 119, 977
Buie, M. W., Olkin, C., McDonald, S., et al. 1993, IAU Circ., 5898
Bus, S. J., & Bowell, E. 1988, IAU Circ., 4684
Bus, S. J., Bowell, E., Harris, A. W., & Hewitt, A. V. 1989, Icarus, 77, 223
Bus, S. J., Buie, M. W., Schleicher, D. G., et al. 1996, Icarus, 123, 478
Bus, S. J., A'Hearn, M. F., Bowell, E., & Stern, S. A. 2001, Icarus, 150, 90
Campins, H., Telesco, C. M., Osip, D. J., et al. 1994, AJ, 108, 2318
Capria, M. T., Capaccioni, F., Coraldini, A., et al. 1996, Planet. Space Sci., 44, 987
Clark, R. N. 1981, JGR, 86, 3074
Clark, R. N., & Lucey, P. G. 1984, JGR, 89, 6341
Davies, J. K., McBride, N., Ellison, S. L., Green, S. F., & Ballantyne, D. R. 1998, Icarus, 134, 213
Draine, B. T., & Lee, H. M. 1984, ApJ, 285, 89
Duffard, R., Lazzaro, D., Pinto, S., et al. 2002, Icarus, 160, 44
Edoh, O. 1983, Ph.D. Thesis, Univ. of Arizona
Fernández, Y. R., Jewitt, D. C., & Sheppard, S. S. 2002, AJ, 123, 1050
Foster, M. J., Green, S. F., & McBride, N. 1999, Icarus, 141, 408
Froidevaux, L., Matthews, K., & Neugebauer, G. 1981, Icarus, 46, 18
Hapke, B. 1993, Theory of reflectance and emittance spectroscopy (Cambridge University Press)
Hartmann, W. K., Tholen, D. J., Meech, K. J., & Cruikshank, D. P. 1990, Icarus, 83, 1
Jewitt, D., & Luu, J. 1992, AJ, 104, 398
Jewitt, D., & Kalas, P. 1998, ApJ, 499, L103
Jewitt, D., & Fernandez, Y. 2001, Physical properties of Planet-Crossing Objects, 261, 143
Johnson, R. 1991, JGR, 96, 17553
Julian, W. H., Samarasinha, N. H., & Belton, M. J. S. 2000, Icarus, 144, 160
Khare, B. N., Thompson, W. R., Sagan, C., et al. 1990, Lunar and Planetary Institute Conference Abstracts, 21, 627
Kieffer, H., Martin, T., Peterfreund, A., et al. 1977, JGR, 82, 4249
Kiss, C., Ábrahám, P., Klaas, U., Juvela, M., & Lemke, D. 2001, A&A, 379, 1161
Klinger, J., Levasseur-Regourd, A. C., Bouziani, N., & Enzian, A. 1996, Planet. Space Sci., 44, 637
Kowal, C. T. 1996, Asteroids: their nature and utilization (2d ed. New York: Wiley)
Lagerros, J. S. V. 1998, A&A, 332, 1123
Lamy, P. L., Toth, I., Jorda, L., et al. 2002, Icarus, 156, 442
Lamy, P. L., Toth, I., Fernandez, Y., & Weaver, H. A. 2004, COMETS II, ed. M. Festou, H. U. Keller, & H. A. Weaver (University of Arizona Press), in press
Landholt, A. U. 1992, AJ, 104, 340
Lazzaro, D., Florczak, M. A., Betzler, A. S., et al. 1996, Planet. Space Sci., 44, 1547
Lazzaro, D., Florczak, M. A., Angeli, C. A., et al. 1997, Planet. Space Sci., 45, 1607
Lebofsky, L. A., Tholen, D. J., Rieke, G. H., & Lebofsky, M. J. 1984, Icarus, 60, 532
Lebofsky, L. A., Sykes, M. V., Tedesco, E. F., et al. 1986, Icarus, 68, 239
Lebofsky, L. A., & Spencer, J. R. 1989, Radiometry and thermal modeling of asteroids. Asteroids II
Lunine, J., Neugebauer, G., & Jakosky, B. 1982, JGR, 87, 10297
Luu, X. J., & Jewitt, D. C. 1990, AJ, 100, 913
Luu, X. J. 1993, Icarus, 104, 138
Luu, X. J., Jewitt, D. C., & Trujillo, C. 2000, ApJ, 531, L151
Marcialis, R. L., & Buratti, B. J. 1993, Icarus, 104, 234
Meech, K. J., & Belton, J. S. 1990, AJ, 100, 1323
Meech, K. J., Buie, M. W., Samarashina, N. H., Mueller, B. E. A., & Belton, M. J. S. 1997, AJ, 113, 844
Morrison, D., Cruikshank, D. P., Murphy, R. E., et al. 1971, ApJ, 167, L107
Morrison, D. 1976, Icarus, 28, 125
Peixinho, N., Lacerda, P., Ortiz, J. L., et al. 2001, A&A, 371, 753
Peschke, S. 1997, Ph.D. Thesis, University of Heidelberg
Rauer, H., Biver, N., Crovisier, J., et al. 1997, Planet. Space Sci., 45, 799
Roush, T. L. 1994, Icarus, 108, 243
Schmitt, B., Epinasse, S., & Klinger, J. 1991, in 19th luunar and planetary science conference, ed. A. W. Harris, & E. Bowell (Houston: Lunar and Planetary Insitute)
Scotti, J. V. 1997, Minor Planet Circular 1997-D11
Silva, A. M., & Cellone, S. A. 2001, Planet. Space Sci., 49, 1325
Skorov, Yu. V., Kömle, N. I., Markiewicz W. J., & Keller, H. U. 1999, Icarus, 140, 173
Spencer, J. R., Lebofsky, L. A., & Sykes, M. V. 1989, Icarus, 78, 337
Sykes, M. V., & Walker, R. G. 1991, Science, 251, 777
Tholen, D. J., Hartmann, W., & Cruikshank, D. P. 1988, IAU Circ., 4554
Warren, S. G. 1984, Appl. Opt., 23, 1206
West, R. M. 1991, A&A, 241, 635
Winter, D., & Saari, J. 1969, ApJ, 156, 1135
Womack, M., & Stern, S. A. 1997, Proc. Lunar Planet. Sci. Conf. XXVIII, 1575